Impact of Out-of-the-Swath Knowledge on the Antenna Pattern Correction Performance Applied to Conical Scanning Spaceborne Radiometers

Alessandro Lapini, Ada Vittoria Bosisio, *Member, IEEE*, Giovanni Macelloni, *Senior Member, IEEE*, Silvio Varchetta, and Marco Brogioni, *Member, IEEE*

***Abstract*— The future Copernicus Imaging Microwave Radiometer (CIMR), funded by the European Commission and developed by the European Space Agency (ESA), will include a spaceborne radiometer able to provide the highest ground spatial resolution as of launch date for C- to Ka-bands, due to its large deployable mesh reflector able to produce images over a swath 2000 km wide. Because of side and grating lobes in the patterns, the antenna subsystem introduces distortions in the acquired data that result in a loss of radiometric accuracy caused by unwanted energy collected far from the antenna boresight. A candidate antenna pattern correction (APC) algorithm based on an iterative formulation that takes advantages of measurements belonging to the same swath was already proposed by the authors. As the antenna boresight moves closer to the edges of the swath, the antenna pattern (AP) senses regions not already observed, where the correction needs a guess or auxiliary out-of-swath information. This article evaluates the performance of the candidate APC algorithm according to various possible a priori assumptions. Eventually, an evaluation is performed using a timeseries derived from Special Sensor Microwave/Imager enhanced-resolution data. This was done to get a first assessment of the impact of past ancillary information on the APC process.**

***Index Terms*— Antenna pattern correction (APC), Copernicus Imaging Microwave Radiometer (CIMR), conical scan, microwave radiometry, radiometric accuracy.**

I. Introduction

SPACEBORNE microwave radiometers have proven throughout the decades to be an essential tool for the monitoring of Earth processes at a global scale due to their sensitivity to geophysical parameters, accuracy, and possibility to operate independently of daylight conditions. Among the most successful missions for monitoring the surface water cycle worth citing are the Scanning Multichannel Microwave Radiometer (SMMR) on the National Aeronautics and Space Administration (NASA) Nimbus satellite [1], the US Special Sensor Microwave/Imager (SSM/I) of the Defense Meteorological Satellite Program (DSMP) constellation [2], the Advanced Microwave Scanning Radiometer for EOS (AMSR-E) onboard the NASA Aqua satellite [3], and the Advanced Microwave Scanning Radiometer 2 (AMSR2) onboard the Japan Aerospace Exploration Agency (JAXA) Global Change Observation Mission—Water (GCOM-W) [4]. The follow-up of the last sensor will be the Advanced Microwave Scanning Radiometer 3 (AMSR3) onboard the Global Observing SATellite for Greenhouse gases and Water cycle (GOSAT-GW) and will have similar characteristics to those of AMSR2, such as radiometric and ground resolution performances, with the major difference of having two more channels in the mm wavelength spectrum [5]. Along with multichannel missions, worth being cited are also European Space Agency (ESA)'s Soil Moisture and Ocean Salinity [6] and NASA' Soil Moisture Active and Passive [7] satellites, both working only at the L-band. While providing invaluable data to the scientific community, the main weakness of all these spaceborne sensors has always been the ground spatial resolution, on the order of tens of kilometers, which has somewhat limited their application. To tackle this and to ensure a long-term continuity of global-scale passive microwave measurements, the Copernicus Imaging Microwave Radiometer (CIMR) mission has been funded by the European Commission and developed by the ESA [8]. The mission is presently planned for launch in 2028/29 and one of its main characteristics will be the highest ground spatial resolution available for a spaceborne radiometer at C- to Ka-frequencies, from two to three times better than JAXA AMSR2 depending on the specific frequency band. This is going to be achieved by means of a large deployable mesh reflector illuminated by a multifeed array, able to produce images with an almost 2000-km swath and to cover daily the entire surface of the Earth. Despite this important result, it should be considered that the technologies currently available for the reflector do not allow having a pencil-beam antenna pattern (AP) at all frequencies. At the K- and Ka-bands, such antenna subsystem introduces distortions in the acquired data due to the presence of side and grating lobes in the patterns. These unwanted lobes collect energy far from the antenna boresight, causing a loss in radiometric

Received 2 August 2024; revised 7 November 2024 and 26 November 2024; accepted 20 December 2024. Date of publication 25 December 2024; date of current version 15 January 2025. This work was supported by the Thales Alenia Space—Italy in the framework of the Phase C activities of the CIMR mission, a component of the Copernicus Program funded by the European Union and developed by the European Space Agency. *(Corresponding author: Marco Brogioni.)*

Alessandro Lapini, Giovanni Macelloni, and Marco Brogioni are with the National Research Council of Italy, Istituto di Fisica Applicata "N. Carrara," 50019 Sesto Fiorentino, Italy (e-mail: marco.brogioni@cnr.it).

Ada Vittoria Bosisio is with the National Research Council of Italy, Istituto di Elettronica ed Ingegneria dell'Informazione e delle Telecomunicazioni, 20133 Milan, Italy.

Silvio Varchetta is with Thales Alenia Space-Italy, 00131 Rome, Italy.

Digital Object Identifier 10.1109/TGRS.2024.3522515

accuracy. Therefore, it is important to adopt a correction algorithm that corrects for this impairment.

A candidate algorithm for the AP correction (APC) of CIMR acquisitions, which can be applied to any spaceborne conical scanning radiometer, was already introduced in a previous paper [9]. For each acquisition, the algorithm determines the ground region imaged by the AP and estimates the contribution of the front side and grating lobes region using the same acquisitions. Cross-polarization leaks, ohmic losses, and back pattern contribution are compensated for in separate stages in the CIMR processing chain. The algorithm was tested using only measurements collected in the same pass, allowing to perform the correction and to assess the performance in a limited (inner) part of the swath. Nevertheless, near the edges of the swath, the AP side lobes look also out of the swath and auxiliary information is needed to perform the correction. This article aims at evaluating the performance of the devised APC algorithm over the entire swath[1] when such auxiliary information is provided. Furthermore, it introduces a different, more suitable reference AP with respect to the one described in [9] for a benchmark of APC performance. For sake of coherence with the previous work, the presented analysis and results refer to the Ka-band.

The outline of this article is the following. In Section II, the statement of the problem and a summary of the APC algorithm are provided, along with a more suitable reference AP concept. In Section III, the setup for analyzing the performance (test scenarios and metrics used to evaluate the performance of the APC) is introduced. Section IV deals with the testing of the algorithm on synthetic scenarios. A demonstration carried out using real brightness temperature data derived from the SSM/I mission is given in Section V. A discussion and some conclusions are presented in Section VI.

II. Description of the APC

A. Problem Statement

The brightness temperature measured by a spaceborne radiometer while pointing to r is modeled as

$$T_A(r) = \int A(r, r')\, T_b(r')\, dr' + \delta(r) \tag{1}$$

where T_A is the antenna temperature, A is the projection of the AP on the Earth's surface, T_b is the spatial-continuous brightness temperature of the scene, and δ is a nuisance accounting for other contributions, such as back lobes, cross-polarization effects, measurement noise, and nonlinear effects not corrected here. It is possible to rewrite (1) in a more convenient way as

$$T_A(r) = \int_{\mathrm{MB}} A(r, r')\, T_b(r')\, dr + \int_{\mathrm{SP}} A(r, r')\, T_b(r')\, dr' + \int_{\mathrm{TP}} A(r, r')\, T_b(r')\, dr' + \delta(r). \tag{2}$$

In (2), the first integral accounts for the energy collected by the main beam (MB) of the AP (defined as the portion between the boresight and 2.5 times the −3-dB angle); the second integral is computed over the secondary pattern (SP) and indicates the energy to be compensated for by the APC algorithm; the last integral accounts for the energy collected by the tertiary pattern (TP), i.e., the region of the AP below a chosen threshold such that the relative integral is so small that it can be disregarded in the computation of T_A. The purpose of identifying a TP is to decrease the computational costs with an acceptable radiometric impact; therefore, TP thresholds are determined for the specific frequency channel and antenna characteristics. A sketch of these three regions is provided in Fig. 1 top. The MB collects 96% of the energy radiated from the scene. The TP threshold is set to −55.91 dB, corresponding to a maximum theoretical approximation error of 0.05 K. Using this value, the SP (side and grating lobes) accounts for slightly less than 4% and the TP to less than 0.1% of the collected energy of the AP (albeit representing 99.9% of the front antenna pattern). The first ring of grating lobes is 70–100-km distant from the boresight, while the second ring is 160–180-km distant. The aim of the APC algorithm is to correct the antenna temperature for energy contributions coming from the SP. In the CIMR mission, this has to be done in an effective way for each of the samples acquired by the radiometer [8]. The APC algorithm has already been described in [9], thus only a brief overview is given here.

The APC algorithm produces a corrected version of each measurement of T_A (also referred as a sample).

The correction of a sample sensed in a given position (blue ellipsoids in Fig. 2) is achieved using the samples collected during the same orbit, to account for the energy picked up by the SP (small blue and red circles in Fig. 2). The ensemble of the measurements' positions that undergo the correction is called "solving region." The algorithm works iteratively: at each iteration, and the corrected values of the samples in the solving region are updated using the result of the previous iteration. The algorithm is proved to converge if the MB energy accounts for more than 50% of the entire AP. In [7], the solving region was limited to the positions for which the SP is fully enclosed inside the swath (e.g., situation (A) in Fig. 2), so that no out-of-the-swath information was required for the assessment of the performance. In this work, the solving region is extended up to the edges of the swath, including the positions whose corresponding side/grating lobes swipe out-of-the-swath (e.g., small red circles of situations (B) and (C) in Fig. 2). Accordingly, the boundary region is now out of the swath and auxiliary brightness temperature data that account for the out-of-the-swath radiometric scene are required.

While the samples in the solving region are acquired in the instrument geometry and are all collected during the same pass, the ones of the boundary region could have more relaxed requirements as they stem from other CIMR orbits or different sources. First, they are unlikely to be contemporary with the brightness temperature samples under correction (although this is desirable). Furthermore, they can come from various sources such as climatology, brightness temperature data from other

[1]By "entire swath" is meant the full extension of the swath excluding the calibration period, when the sensor does not sense the Earth's surface. CIMR calibration is scheduled at each scanning period when the sensor is close to one edge of the swath.

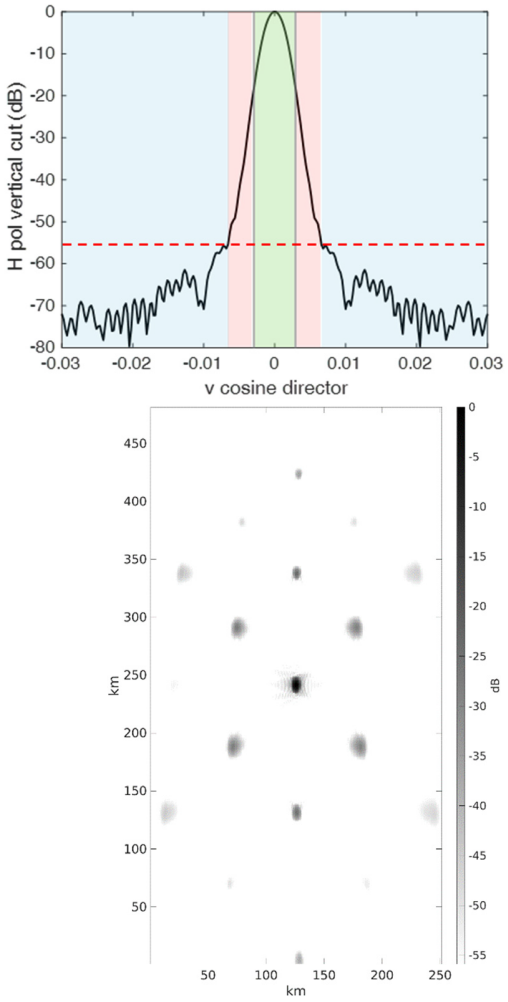

Fig. 1. (Top) Example of vertical cut of the H pol AP at the Ka-band. Green, red, and blue backgrounds represent the MB, the secondary, and TPs, respectively. The horizontal red dashed line represents the TP threshold. (Bottom) AP projected on ground used in the study highlighting side lobes (around the MB) and grating lobes. Values are normalized to AP maximum.

satellite missions, and past sensor acquisitions. Obviously, the correction is expected to be more accurate as the temporal lag between the two kinds of data decreases. Regarding the spatial distribution, the requirement for the boundary region data is that they must be geolocated to allow the implementation of a meshing grid [7]; even though there is no constraint on the spatial grid resolution and displacement, a finer grid has the potential to provide better results.

Some potential data sources for the APC can be the following:

1) A constantly updated mosaic of CIMR samples for each frequency and polarization. After each semiorbit is acquired, old samples are replaced by the newest ones. This is seemingly the best choice because the auxiliary information used is self-coherent, the information provided to the algorithm is always updated and the spatial resolution consistent.
2) A daily or multidaily mosaic of CIMR samples. This solution is computationally cheaper than the constantly updated mosaic; the drawback is a worse representation of those regions undergoing rapid changes (e.g., marginal ice zones).
3) A map created with data acquired by different sensors (e.g., AMSR2, SSM/I). The auxiliary data can be "fresher" than the constantly updated mosaic; however, the intercalibration between sensors and the impact of the different spatial resolutions have to be carefully evaluated.
4) A multiweekly or monthly mosaic of CIMR brightness temperature data. This is the computationally cheapest solution. Although it can provide acceptable information for land and water targets, it is not expected to work well for dynamic scenarios such as sea ice that can evolve on a daily basis.

It is worth remarking that the data source does not influence the APC algorithm workflow because this does not depend on the source of the information. It only impacts the attainable correction performance.

B. Realistic Versus Ideal APs

In this study, an example of a realistic CIMR Ka-band AP is considered whose ground projection is depicted in Fig. 1 bottom, where the presence of side and grating lobes is visible. This AP is fed into the simulator to generate the realistic CIMR measurements, which then undergo the proposed APC. Since the MB accounts for about 96% of the energy, the proposed APC algorithm converges and it can be applied to correct for the secondary and grating lobes. To assess the effectiveness of the APC, reference measurements must also be simulated. They are generated following the same process of the realistic measurements but replacing the realistic AP with an "ideal" one and removing the APC stage. The reference measurements are also referred to as "ideal" measurements in the CIMR mission. Intuitively, the closer the output of the APC to the ideal measurements, the better the correction.

The definition of the ideal AP is pivotal for assessing APC performance, and different choices are possible. In the initial phases of the CIMR mission (and in [9]), it was assumed that the ideal pattern had a uniform gain inside a given solid angle and zero elsewhere. However, this has been later deemed unrealistic. As a novelty of this work, the "shape-preserving" ideal AP is introduced and used in place of the uniform ideal AP. A visual comparison of the two ideal APs is depicted in Fig. 3. The shape-preserving AP has the same shape as the realistic AP inside the MB and is zero in the SP and TP, that is, it has no side or grating lobes. The MB of the shape-preserving AP is normalized to account for the removed energy. In formula

$$\mathrm{AP}_{\mathrm{ideal}}(\theta,\phi)=\begin{cases}\dfrac{\mathrm{AP}(\theta,\phi)}{\iint_{\mathrm{MB}}\mathrm{AP}(\theta',\phi')}, & (\theta,\phi)\in\mathrm{MB}\\ 0, & \text{elsewhere}\end{cases}$$

where AP and $\mathrm{AP}_{\mathrm{ideal}}$ are the AP and the shape-preserving AP, respectively, and (θ,ϕ) are the spherical coordinates in the antenna reference frame.

Comparing the shape-preserving AP with the uniform AP, the former preserves the response of the real antenna and,

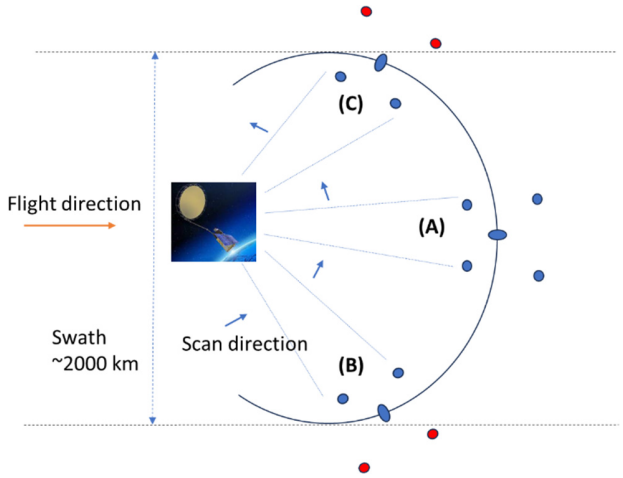

Fig. 2. Sketch of the conical scanning acquisition mechanism. Circles in positions (A)–(C) represent the MB and grating lobes of the AP ground projection: in blue when they are inside of the radiometer swath, in red when outside.

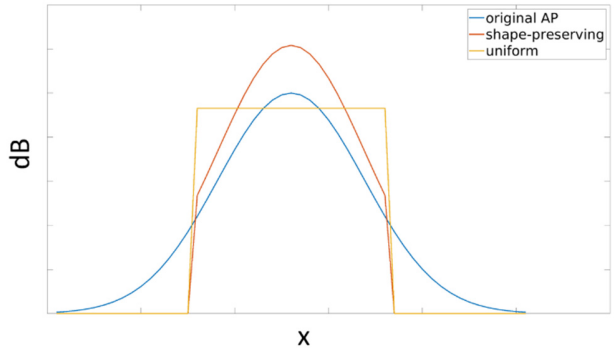

Fig. 3. Qualitative comparison between the uniform (used in [7]) and the shape-preserving AP (presented and used in this work). The support of both corresponds to the MB of the realistic AP (indicated as "original AP"). The APs' energy is the same.

consequently, it is more focused inside the MB region; due to this peculiarity, it is used in this work.

III. Performance Analysis Setup

To evaluate the impact of the ancillary information on the performance of the APC, some relevant synthetic scenarios were devised as stress tests for this method. The aim was to determine the order of magnitude of the APC errors and their spatial distribution when the auxiliary information is both radiometrically and spatially incorrect. Then, an application of the APC algorithm to real data will be presented in Section V, providing a preview of the performances in a potential actual case.

A. Synthetic Scenarios

Three different scenarios are chosen to test the APC algorithm at the edges of the swath in the Ka-band H-pol. In all of them, the flight direction is assumed left-to-right, parallel to the upper/bottom border of the scene and counterclockwise scanning as in Fig. 2.

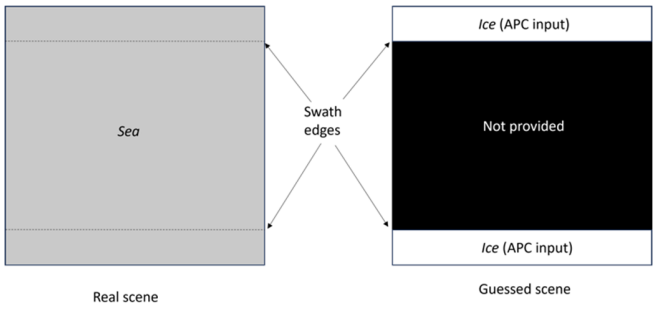

Fig. 4. Test scenario (A): all-sea/ice. (Left) True scene that is sensed. (Right) Scene provided to the APC. It is "wrongly" supposed that there is ice instead of sea water in the boundary region stripes above and below the edges of the swath.

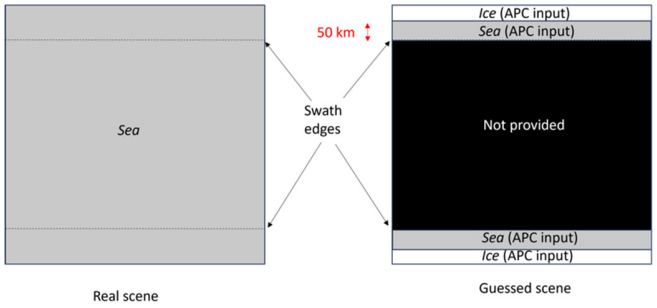

Fig. 5. Test scenario (B): all-sea/shifted-ice. (Left) True scene that is sensed. (Right) Scene that is guessed before the APC is applied. Unlike Fig. 4, the first 50 km close to the edges of the swath is correctly assumed to be sea water.

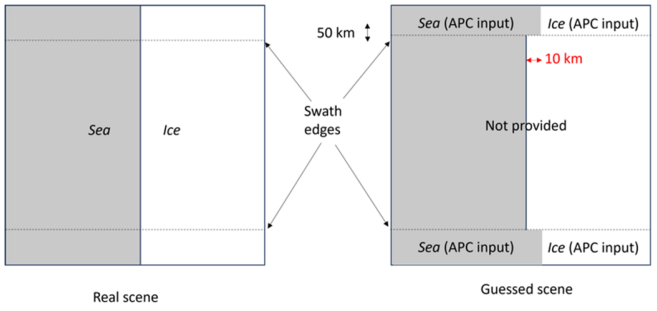

Fig. 6. Test scenario (C): drifting ice. (Left) True scene that is imaged by CIMR. (Right) Scene that is assumed before the APC is applied. There is a 10-km offset between the true and guessed transitions from sea to ice. The transition inside the swath is depicted only to highlight the 10-km offset.

(A) A uniform scene with $\boldsymbol{T_b} = 135$ K representative of the open sea (this value of $\boldsymbol{T_b}$ was chosen so as to be coherent with [9] and with the requirements of the CIMR [8]) and the APC algorithm was fed with wrong auxiliary information: the presence of sea ice out of the swath was assumed with $\boldsymbol{T_b} = 250$ K (Fig. 4).

(B) Like scenario (A), but the information outside of the swath consists of two stripes of sea water 50 km wide in the across-swath direction (correct auxiliary information) and then ice (wrong auxiliary information) (Fig. 5).

(C) A transition scenario (sea/ice) perpendicular to the flight direction; it is wrongly assumed that the sea–ice transition is shifted along-track by 10 km with respect to the actual one (Fig. 6).

(D) A scenario like (C), but the sea–ice transition is shifted along-track by 20 km.

Scenarios (A) and (B) allow gauging the performance of the APC in the presence of a strong radiometric mismatch between the actual boundary conditions and the guessed ones. Scenarios (C) and (D) are devised to assess the impact of a geometric mismatch between the actual and the auxiliary information provided to the APC. Specifically, they are conceived to evaluate the impact of using outdated information (e.g., the actual position of marginal sea–ice boundary is offset with respect to the available out-of-the-swath auxiliary information). It is worth noting that the sea/ice transition is not the strongest on Earth; for instance, bare soil and vegetation can have a much higher T_b (up to about 300 K) so that a coastal transition (sea/Earth) leads to a higher contrast.

The reason for using open sea and sea–ice brightness temperatures is due to their being the main targets of the CIMR mission [8]. Furthermore, the geolocation of land coastal borders can be considered spatially stable at the kilometer scale during the life of the satellite; this is not true for sea water/sea–ice transitions (e.g., marginal ice regions), thus making these the most challenging context for the APC.

B. Performance Metrics

The main quantity with which to assess the performance of the APC algorithm is the APC error, defined as

$$e_{\mathrm{APC}} = T_{A_{\mathrm{corr}}} - T_{A_{\mathrm{ideal}}} \tag{3}$$

where

$$T_{A_{\mathrm{corr}}} = \mathrm{APC}(T_A) \tag{4}$$

is the output of the APC algorithm when realistic measurements T_A are provided as input, and $T_{A_{\mathrm{ideal}}}$ is the brightness temperature that would have been sensed by the instrument if the ideal AP was used in lieu of the actual one and no APC processing was applied.

The metric used in the CIMR mission for the APC is the success rate, SR, defined by

$$\mathrm{SR} = \frac{100}{N}\sum_{n=0}^{N-1}\begin{cases}1, & \text{if } \left|T_{A_{\mathrm{corr}}}[n] - T_{A_{\mathrm{ideal}}}[n]\right| < 0.5 \text{ K} \\ 0, & \text{otherwise}\end{cases} \tag{5}$$

where N is the number of samples in the solving region and n indicates their position in the CIMR sampling grid. The metric is the percentage of points for which the absolute estimation error is less than 0.5 K. The threshold is chosen according to [8] (OBS-1040).

The measurements belonging to a central region of each scenario are considered for evaluating the performance. Such a region is 500-km wide and about 2000-km high, to account for the maximum extension of the considered AP in the along-scan direction and the swath in the across-scan direction, respectively. For sake of analysis, samples are grouped according to their distance from the closest edge of the swath, as depicted in Fig. 7. For scenarios (C) and (D), measurements are also grouped according to their distance from the sea–ice transition. Pixels 1 × 1 km are used in all the scenarios. By convention, distances are quantized at 1 km using truncation (e.g., distances below 1 km are reported as 0 km).

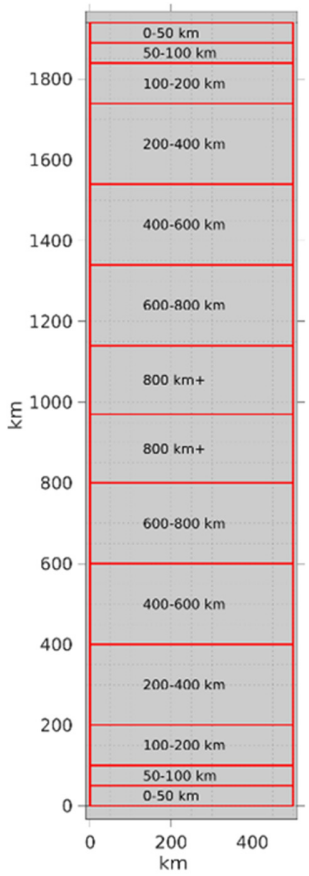

Fig. 7. Performance evaluation region (outermost rectangle), divided in ranges of distances from the closest edge of the swath (inner rectangles).

IV. Results on Synthetic Scenarios

The first results presented are related to the impact of a radiometric mismatch between the actual and assumed auxiliary information. Fig. 8 depicts the spatial distribution of the APC error in scenarios (A) and (B), near the top (top row) and bottom (bottom row) edges of the swath. For the sake of clarity, errors smaller than ±0.5 K are not represented. The results in the central part of the swath are omitted because they are inside the interval ±0.5 K.

In scenario (A), the "compliant correction border" is about 70 and 64 km from the top and bottom edges, respectively; it decreases to 22 and 5 km in (B) scenario because the information provided to the algorithm is more consistent with the true scene. All the error values are negative because the APC is deceived using a value that is higher (ice) than the real one (sea), so the APC overcompensates. As a result, the corrected brightness temperature is lower than the ideal brightness temperature. The magnitude of the maximum error does not exceed 2 K for scenario (A) and 1 K for scenario (B). The asymmetry of the error near the edges is due to the calibration period that affects the top edge, reducing the number of acquired samples.

Table I reports the success rate achieved by the APC in (A) and (B) scenarios. Each row refers to a specific range of distances from the edges of the swath (see Fig. 7). For instance, in the range 0–50 km, only the samples belonging to

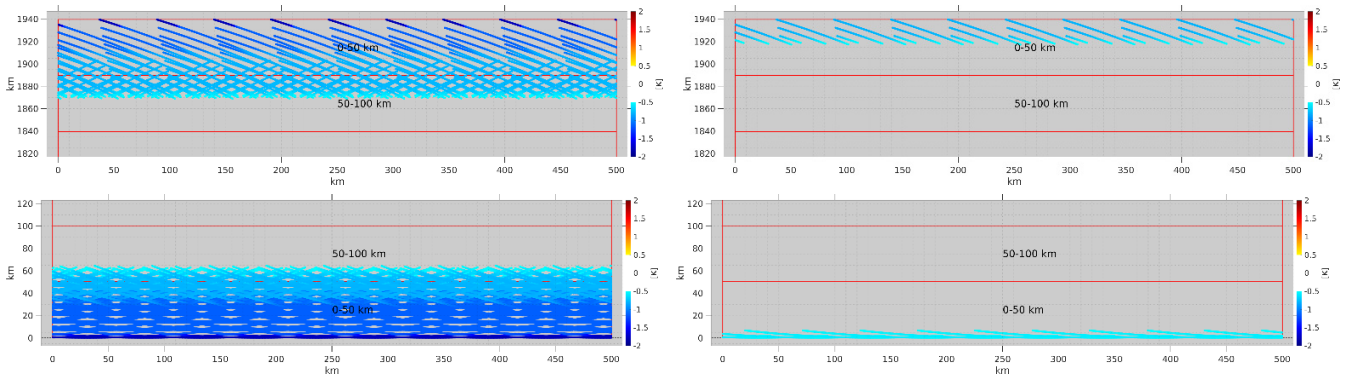

Fig. 8. APC error for the all-sea/ice scenario (A), left column, and all-sea/shifted-ice scenario (B), right column. The top row represents the left region of the swath, while the bottom row shows the right region. For the sake of clarity, errors below 0.5 K are not reported. The red lines delimit the ranges of distance and correspond to the ones depicted on the top (respectively, bottom) of Fig. 7. Note that the calibration period affects the upper region of the swath.

TABLE I

SUCCESS RATE FOR THE ALL-SEA/ICE AND ALL-SEA/SHIFTED ICE CASES, PARTITIONED ACCORDING TO THE DISTANCE FROM THE CLOSEST EDGE OF THE SWATH

Distance from swath edge (km)	Success Rate (%)	
	All-sea/ Ice	All-sea/ Shifted-Ice
0-50	0	92.6
50-100	69.4	100
100-200	100	100
200-400	100	100
400-600	100	100
600-800	100	100
+800	100	100

the top and to the bottom rectangles of Fig. 8 are considered. Analogously, the range 800 km+ considers the samples in the middle of the swath.

Since (A) scenario represents the worst case in terms of radiometric mismatch, we can conclude that APC is capable of containing the possible "contaminations" from a wrong knowledge of the boundary conditions within 100 km from the swath. The "compliant correction border" moves from 100 to 50 km in the all-sea/shifted-ice scenario, in accordance with the fact that the guessed sea–ice transition moves outward by the same distance. This highlights the importance of the quality of the auxiliary information for limiting the correction errors.

The impact of a geometric mismatch in the auxiliary information is evaluated in the drifting ice scenario (C). In Fig. 9, the spatial distribution of the APC error near the edges swath is depicted. At the top edge (Fig. 9—top), where there are fewer samples due to the calibration period, it can be seen that the influence of the drifting ice is limited to within 6 km. At the bottom edge (Fig. 9—bottom), the impact is higher and extends up to 50 km. Nevertheless, the mission requirements for performance evaluation contemplate a "don't care region" of 1.5 footprint (which corresponds to from 6 to 7.5 km, according to which value of the footprint is adopted [8]) from the radiometric transition. In this respect, the impact at the bottom edge is below 4 km. The maximum error in this scenario is below 1.1 K.

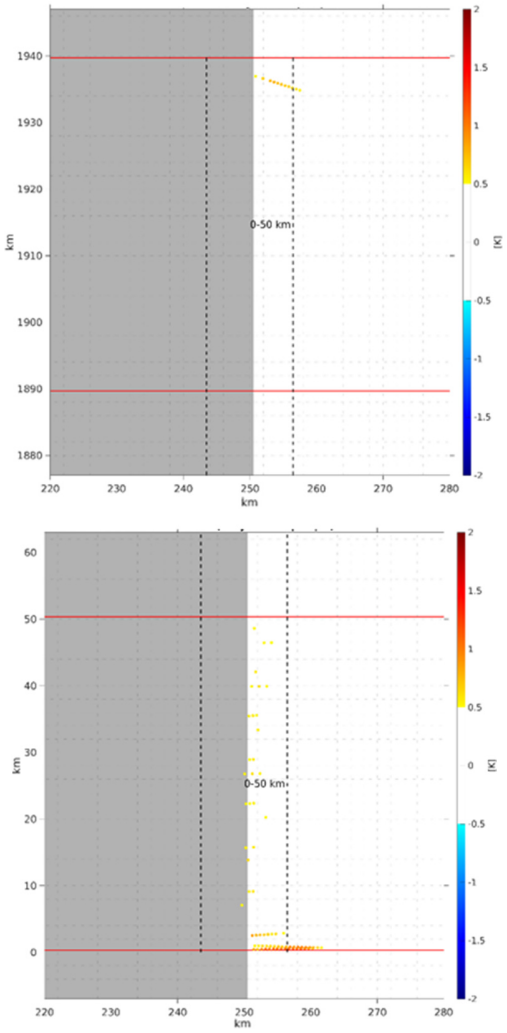

Fig. 9. APC error on the 10-km drifting ice scenario near the top edge of the swath (top) and near the bottom edge of the swath (bottom). For the sake of clarity, no errors below 0.5 K are reported. The black dashed lines delimit the ±6.0-km zone around the transition.

The numerical results obtained for the APC performance are reported in Table II. The cells indicate the success rate within a given range of distances from the closest edge of the

TABLE II

SUCCESS RATE (%) FOR THE 10-km DRIFTING ICE SCENARIO, PARTITIONED ACCORDING TO THE DISTANCE FROM THE CLOSEST EDGE OF THE SWATH (ROWS) AND FROM THE TRANSITION (COLUMNS)

Distance from swath edge (km)	Distance from the transition (km)								
	0-4	4-5	5-6	6-7	7-8	8-10	10-20	20-50	50+
0-50	96	97.5	97.9	98.6	98.9	98.9	99.8	100	100
50-100	100	100	100	100	100	100	100	100	100
100-200	100	100	100	100	100	100	100	100	100
200-400	100	100	100	100	100	100	100	100	100
400-600	100	100	100	100	100	100	100	100	100
600-800	100	100	100	100	100	100	100	100	100
+800	100	100	86.9	100	100	100	100	100	100

TABLE III

SUCCESS RATE (%) FOR THE 20-km DRIFTING ICE SCENARIO, PARTITIONED ACCORDING TO THE DISTANCE FROM THE CLOSEST EDGE OF THE SWATH (ROWS) AND FROM THE TRANSITION (COLUMNS)

Distance from swath edge (km)	Distance from the transition (km)								
	0-4	4-5	5-6	6-7	7-8	8-10	10-20	20-50	50+
0-50	97.1	97.8	97.9	98.6	98.2	98	98.8	100	100
50-100	99.1	100	100	100	100	100	100	100	100
100-200	100	100	100	100	100	100	100	100	100
200-400	100	100	100	100	100	100	100	100	100
400-600	100	100	100	100	100	100	100	100	100
600-800	100	100	100	100	100	100	100	100	100
+800	100	100	86.9	100	100	100	100	100	100

swath (rows) and within a given range of distances from the vertical transition (columns).

The red vertical delimiters highlight the position of a distance of 1.5 footprint from the transition, in the cases where the size of the footprint is 4 and 5 km, respectively (in the latter case, rounding is applied). It emerges that the APC attains a compliant correction at any distance from the transition except the range 0–50 km, which is influenced by the mismatch of the boundary conditions. In other terms, the mismatch due to the drifting ice influences the results at most 50 km from the swath edge and at most 10 km from the vertical transition. Incidentally, the latter corresponds to the extension of the drift.

By comparing the success rate of the APC algorithm applied to the two different ice drifting cases (Tables II versus III), small variations are appreciable in the 0–50-km distance range and in the 50–100-km distance range. If the same cross-check is performed on the spatial distribution of the APC error (Figs. 9 versus 10), it can be noted that the actual effect of the mismatch extends up to 22 km from the transition and about 3–4 km above the edge of the swath.

The same experiment is carried out also by increasing the difference between the actual and guessed boundary conditions, scenario (D). Specifically, the drift ice (20 km) is a modified target scene where the drift is extended from 10 to 20 km. The success rate for this case is shown in Table III, and the APC error is shown in Fig. 10.

V. APPLICATION OF APC TO REAL DATA

The analysis described in the previous section (as well as the one carried out in [9]) has been performed by feeding the forward model, i.e., the "radiometer simulator," with synthetic input scenes at 1-km ground resolution. When it comes to data acquired from space, there is no available dataset at the 1-km scale. Nevertheless, it is possible to find reprocessed products with improved resolution obtained by leveraging

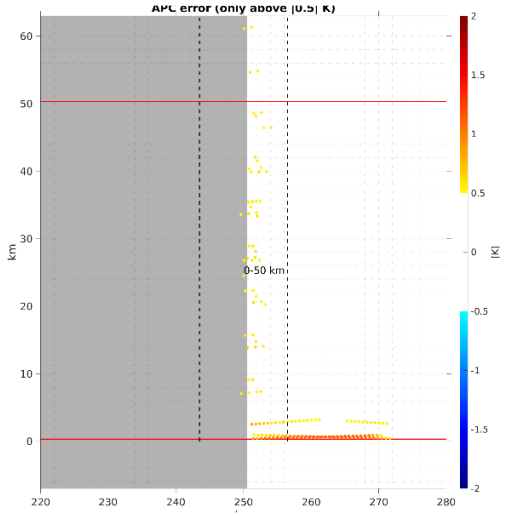

Fig. 10. APC error on the 20-km drifting ice scenario near the bottom swath edge. For the sake of clarity, errors below 0.5 K are omitted. The black dashed lines delimit the ±6.0-km zone around the transition.

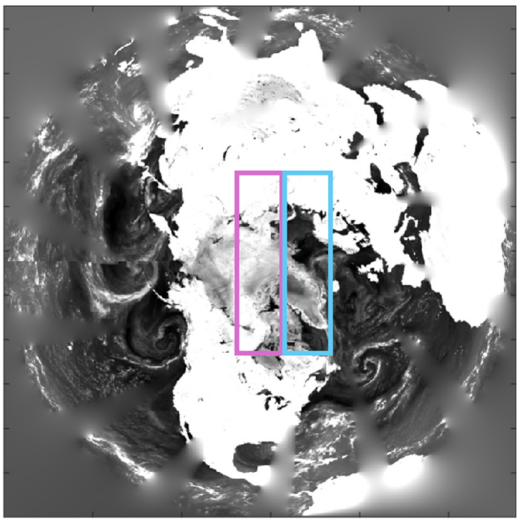

Fig. 11. *H* pol Ka-band mosaic of F18 SSM/I morning overpasses at enhanced resolution used for testing the APC. The purple and cyan boxes indicate the regions undergoing the APC.

multiple overpasses over a given region. This is the case for the MEaSUREs calibrated enhanced-resolution passive microwave daily EASE-grid 2.0 brightness temperature Earth System Data Record [10]. This product is distributed by the NASA NSIDC and consists of calibrated enhanced-resolution brightness temperature datasets of several sensors (e.g., SMMR, SSM/I, AMSR-E). We chose to use a daily mosaic of SSM/I data collected at the Ka-band over the boreal region at 3.125-km ground resolution. The enhancement of the resolution is obtained by applying the radiometer version of the Scatterometer Image Reconstruction (rSIR) Algorithm [11], [12]. In this context, the NSIDC 0630 products are used assuming that the ground resolution is 1 km. Even though not strictly realistic, this choice preserves the fluctuations in T_b that would be smoothed away by any interpolation aiming at further improving the ground resolution.

The setup of the test is the following. The dataset collected the morning of July 2, 2023 by the F18 SSM/I sensor is selected as the one to be corrected (Fig. 11). Then, data

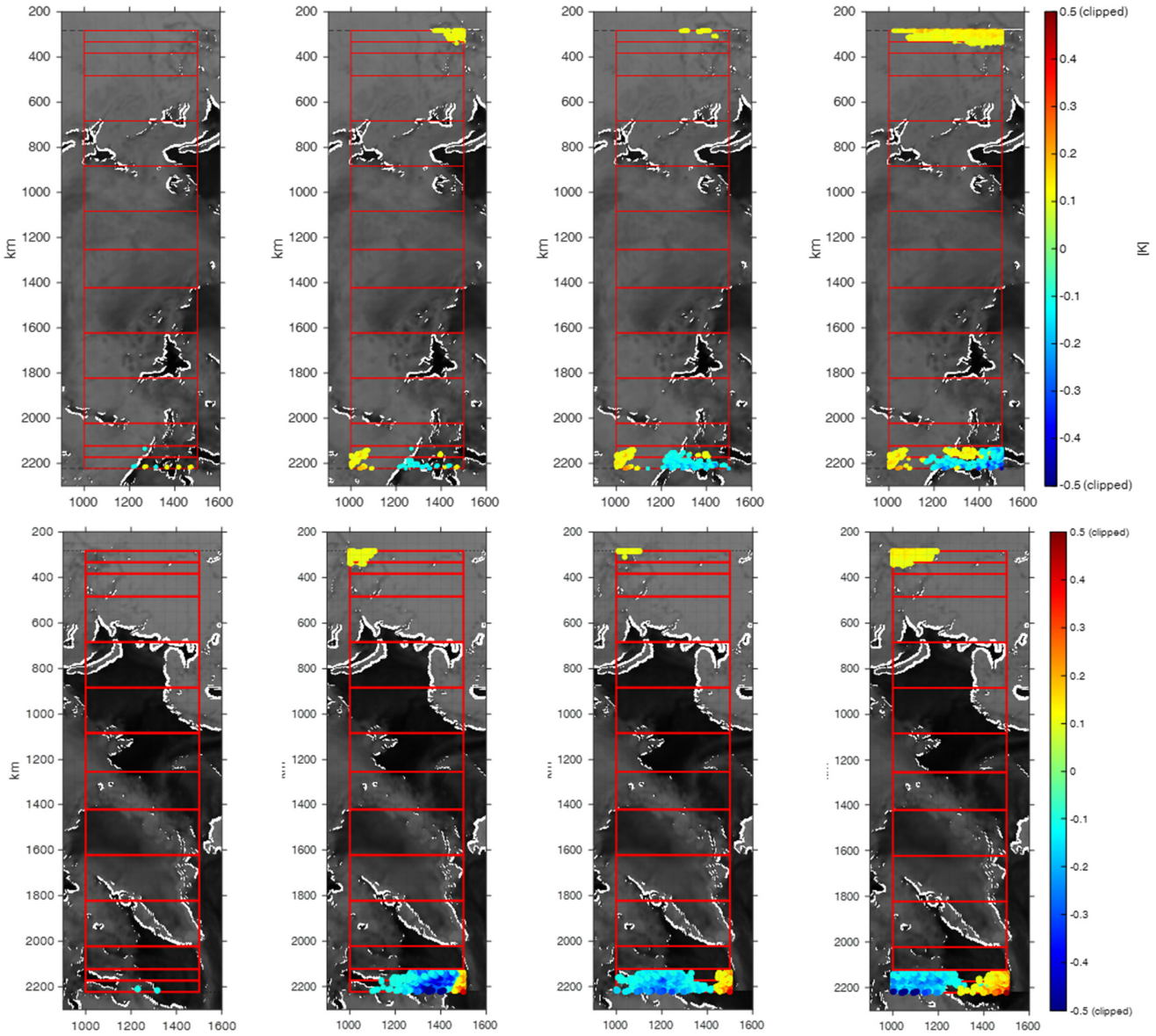

Fig. 12. APC correction errors obtained using the auxiliary information collected the same day (left column), one day before (center left column), two days before (center right column), and one week before (right column). Top and bottom panels refer to the purple and blue boxes of Fig. 11, respectively. The outer rectangle in the top (respectively, bottom) row's images corresponds to the left (respectively, right) box depicted in Fig. 11, whereas the inner rectangles indicate the range of distances from an edge of the swath.

collected the same day as well as 1, 2, and 7 days before are used as out-of-the-swath auxiliary information for the APC. Both the H and V polarizations are processed (for the sake of conciseness, only the former is shown). Void pixels in the mosaics of the datasets were filled using a suitable interpolation routine [13].

The purple and cyan boxes in Fig. 11 represent the regions undergoing APC. Due to the limitations of hardware computing, the two 2000 × 500 km regions are separately processed by the APC. The two regions have been chosen because they encompass the main targets of the CIMR mission (i.e., sea ice, permafrost, and ice sheets).

Despite rSIR spatial resolution enhancement, the selected SSM/I data do not show strong discontinuities, likely due to the smoothing effect of the sensor antenna footprint. Thus, the sharpness of the synthetic data is partially lost and is difficult to be visually identified. In the following images, the discontinuities with a change in T_b equal or greater than 10 K are highlighted with white bold lines.

Fig. 12—top shows the correction errors obtained when the APC is applied to H polarization North-Pole-centered brightness temperature data (purple box in Fig. 11) with out-of-the-swath auxiliary information collected the same day or 1, 2, and 7 days earlier; Fig. 12—bottom shows the results when the region centered over Greenland is considered (blue box in Fig. 11). Errors smaller than ±0.1 K are not shown. To begin with, note that the errors are localized near the edges of the swath. Second, the APC error increases as the auxiliary information gets older. This is particularly evident in the Hudson Bay region, Canada, over which few and small errors are already present when using the same day auxiliary information (Fig. 12—top panel). As expected, the older the auxiliary

information, the higher and more spread the APC error at the edges; however, its magnitude never exceeds 0.5 K. The same effects can be seen by considering the V polarization dataset (not shown here). When it comes to analyzing the results of the APC algorithm applied to the Greenland-centered region (cyan box of Fig. 11), the results look similar, although the APC error of some pixels along the bottom edge of the swath (over Canada) reaches -0.57 K at the V pol for the case of a 1-week-old auxiliary information (Fig. 12—bottom panel). In all the considered cases, the magnitude of APC errors is above 0.1 K only in the first 50 km from the edges of the swath. The success rate is 100% in any other subregion considered.

VI. Discussion and Conclusion

The present article aims at completing the assessment of the APC algorithm designed for potential use in the CIMR mission. While [9] was focused on the description of the algorithm and its performance when operating in the central swath, this article explores the feasibility of extending the application of the APC algorithm to the entire swath. In Section IV, the worst case of the correction is evaluated by misleading the algorithm, i.e., providing completely wrong auxiliary information that forces a strong overcorrection. Here it is shown that the error introduced is limited in magnitude to a few Kelvin (less than 3 K) and propagate toward the inner part of the swath for less than 50 km. It is remarked that this result depends on the AP; for instance, if there were more energetic side/grating lobes extending farther from the boresight, the error would have propagated to the inner part of the swath. Nevertheless, the present analysis shows that the APC algorithm can work quite successfully over the entire swath without modifications.

The results also show the influence of outdated auxiliary information over fast changing scenarios. This is the case of polar regions, where the marginal sea ice can drift many kilometers per day. The analysis pointed out that the associated error is still quite limited in magnitude and that it propagates toward the center of the swath comparably for the same extent of the ice drift. This fact highlights the importance of having up-to-date auxiliary information when the APC is applied to fast-changing scenarios.

A last conclusion can be drawn from the test performed with real data (Section V), where the radiometric discontinuities are smoother than with synthetic scenarios. The magnitude of APC error is greatly reduced, being appreciable only near the edges of the swath when the auxiliary information is quite outdated. This improvement is inherently due to the low-pass effect of the km-scale ground resolution of spaceborne radiometers, which tend to soften strong fluctuations of the brightness temperature.

A full assessment of the APC will be performed in the forthcoming months, when the end-to-end simulator of the mission will be available and the AP will reach a consolidated status due to the improved TRL.

Acknowledgment

Views and opinion expressed are, however, those of the authors only. The European Commission, and/or ESA and/or Thales Alenia Space cannot be held responsible for any use which may be made of the information contained therein.

References

[1] P. Gloersen and F. Barath, "A scanning multichannel microwave radiometer for Nimbus-G and SeaSat-A," *IEEE J. Ocean. Eng.*, vol. JOE-2, no. 2, pp. 172–178, Apr. 1977, doi: 10.1109/JOE.1977.1145331.

[2] J. P. Hollinger, J. L. Peirce, and G. A. Poe, "SSM/I instrument evaluation," *IEEE Trans. Geosci. Remote Sens.*, vol. 28, no. 5, pp. 781–790, Sep. 1990, doi: 10.1109/36.58964.

[3] T. Kawanishi et al., "The advanced microwave scanning radiometer for the Earth observing system (AMSR-E), NASDA's contribution to the EOS for global energy and water cycle studies," *IEEE Trans. Geosci. Remote Sens.*, vol. 41, no. 2, pp. 184–194, Feb. 2003, doi: 10.1109/TGRS.2002.808331.

[4] K. Imaoka et al., "Global change observation mission (GCOM) for monitoring carbon, water cycles, and climate change," *Proc. IEEE*, vol. 98, no. 5, pp. 717–734, May 2010, doi: 10.1109/JPROC.2009.2036869.

[5] M. Kachi et al., "The advanced microwave scanning radiometer 3 (AMSR3) onboard the global observing satellite for greenhouse gases and water cycle (GOSAT-GW) toward long-term water cycle monitoring," in *Proc. IEEE Int. Geosci. Remote Sens. Symp. (IGARSS)*, Jul. 2023, pp. 561–564, doi: 10.1109/IGARSS52108.2023.10282052.

[6] Y. H. Kerr et al., "The SMOS mission: New tool for monitoring key elements ofthe global water cycle," *Proc. IEEE*, vol. 98, no. 5, pp. 666–687, May 2010, doi: 10.1109/JPROC.2010.2043032.

[7] D. Entekhabi et al., "The soil moisture active passive (SMAP) mission," *Proc. IEEE*, vol. 98, no. 5, pp. 704–716, May 2010, doi: 10.1109/JPROC.2010.2043918.

[8] *Copernicus Imaging Microwave Radiometer (CIMR) Mission Requirements*, document ESA-EOPSM-CIMR-MRD-3236, Feb. 11, 2023.

[9] A. Lapini, A. V. Bosisio, G. Macelloni, and M. Brogioni, "An antenna pattern correction algorithm for conical scanning spaceborne radiometers: The CIMR case," *IEEE Trans. Geosci. Remote Sens.*, vol. 61, 2023, Art. no. 5300215, doi: 10.1109/TGRS.2023.3238269.

[10] M. J. Brodzik and D. G. Long, 2016, "MEaSUREs calibrated enhanced-resolution passive microwave daily EASE-Grid 2.0 brightness temperature ESDR, version 1," NASA Nat. Snow and Ice Data Center Act. Arch. Center, doi: 10.5067/MEASURES/CRYOSPHERE/NSIDC-0630.001.

[11] D. G. Long and M. J. Brodzik, "Optimum image formation for spaceborne microwave radiometer products," *IEEE Trans. Geosci. Remote Sens.*, vol. 54, no. 5, pp. 2763–2779, May 2016, doi: 10.1109/TGRS.2015.2505677.

[12] D. G. Long, M. J. Brodzik, and M. Hardman, "The effective resolution of CETB image products," Nat. Snow Ice Data Center, Boulder, CO, USA, Tech. Rep. 21, May 2021. [Online]. Available: https://nsidc.org/sites/default/files/nsidc-special-report-21.pdf

[13] J. D'Errico. (2024). *Inpaint_nans*. MATLAB Central File Exchange. [Online]. Available: https://www.mathworks.com/matlabcentral/fileexchange/4551-inpaint_nans

Alessandro Lapini received the M.Sc. degree (Hons.) (summa cum laude) in telecommunications engineering and the Ph.D. degree in computer science, systems and telecommunications from the University of Florence, Florence, Italy, in 2010 and 2014, respectively.

Since 2014, he has been a Research Assistant at the University of Florence, where he was initially with the Department of Information Engineering and then with the Department of Industrial Engineering since 2015. From 2016 to 2018, he was a Research Fellow with the Department of Industrial Engineering, University of Florence. Since 2019, he has been with the Microwave Remote Sensing Group, Institute of Applied Physics Nello Carrara (IFAC), Consiglio Nazionale delle Ricerche (CNR), Florence. His research interests are focused on signal and image processing, particularly in the field of remote sensing and biomedical imaging, acoustics, and active noise control.

Ada Vittoria Bosisio (Member, IEEE) received the M.S. degree in electronic engineering and the Ph.D. degree in applied electromagnetism from the Politecnico di Milano, Milan, Italy, in 1991 and 1995, respectively.

For her Ph.D. degree, she was involved in the Olympus and Italsat propagation experiments for the aspects related to propagation-oriented radiometry (Ka-band). From 1995 to 1997, she was a Research Associate with the CETP/CNRS Laboratory, Vélizy, France, where she has been active in the measurement and analysis of forest attenuation and scattering at 2 and 6 GHz. From 1997 to 1998, she was with CNET/France Telecom, Issy Les Mx., France, as an Ingenieur de Recherche, working on the effects of radio waves induced by GSM on the environment and on individuals. From 1999 to 2001, she was with the Propagation Group, Politecnico di Milano, as a Research Associate, working on satellite links at low elevation angle in the K- and W-bands and on propagation of TV broadcast and digital radio links over mountains through ray techniques. Since 2001, she has been a Researcher with the Italian National Research Council, IEIIT Institute, Milan, working on remote sensing applications related to atmospheric science and tropospheric propagation. Her research interests include microwave radiometry and the interaction mechanisms between signal and complex media in the terrestrial biosphere.

Giovanni Macelloni (Senior Member, IEEE) received the M.Sc. degree in electronic engineering from the University of Florence, Florence, Italy, in 1993.

Since 1995, he has been working at the Institute of Applied Physics-CNR-Florence, Florence, where he is now the Head of Research. Since 2019, he has been an Adjunct Professor at the University of Venice, Venice, Italy. His research interests include microwave active and passive remote sensing for the study of the Earth system and cryosphere in particular. He is also involved in the design and development of microwave remote sensing systems from the ground, the air, and satellites. His research has been carried out in the framework of several national and international programs granted by Italian entities, and the European Community and Space agencies (ESA, ASI, NASA and JAXA) and includes the participation in international teams for the studying of the cryosphere and the development and assessment of future spaceborne missions.

Mr. Macelloni is a member of the Cryonet Team of the Global Cryosphere Watch of the WMO, and of the Italian Scientific Antarctic Commission, which implements the national Antarctic program. He has worked as a tutor of Ph.D. students, served as a reviewer for several international committees, organizations, and international journals, and acted as an organizer and a Co-Chair of international conferences. He is an Associate Editor of IEEE TRANSACTIONS ON GEOSCIENCE AND REMOTE SENSING (TGRS).

Silvio Varchetta received the M.Sc. degree in electronic engineering from the University of Rome "La Sapienza," Rome, Italy, in 2002.

From 2003 to 2004, he collaborated with the Microwave Remote Sensing Group, Institute of Applied Physics Nello Carrara (IFAC), Consiglio Nazionale delle Ricerche (CNR), Florence, Italy, with a research grant on behalf of the Istituto di Fisica Applicata "N.Carrara"-IFAC carried out with Alenia Spazio S.p.A., Rome, on the "Study on Active and Passive Polarimetric Sensors for Microwave Satellite Remote Sensing" within the Hydropol Project. Since 2004, he has been a System Engineer working at TAS, Rome, in the field of radiometry payloads involved as technical responsible for ENVISAT/MWR in-flight monitoring, feasibility studies (GPM Br Fr, FLORAD), and phase A/B1 project (Sentinel 3, METOP SG/MWI and ICI, CRYSTAL, CIMR).

Marco Brogioni (Member, IEEE) received the M.Sc. degree in telecommunications engineering from the University of Siena, Siena, Italy, in 2003, and the Ph.D. degree in remote sensing from the University of Pisa, Pisa, Italy, in 2008.

Since 2004, he has been with the Microwave Remote Sensing Group, Institute of Applied Physics Nello Carrara (IFAC), Consiglio Nazionale delle Ricerche (CNR), Florence, Italy. From 2006 to 2007, he was a Visiting Student at the University of California at Santa Barbara, Santa Barbara, CA, USA. His research interests include passive and active microwave remote sensing applied to snow using satellite and ground-based data, especially regarding the development of electromagnetic models for passive and active microwave remote sensing of snow, vegetation, and soil. He is also involved in the design and manufacturing of microwave radiometers (P- to Ka-bands). He is currently involved in several international projects regarding the polar regions.

Dr. Brogioni was a recipient of the Third Prize at the URSI GA Student Prize Paper Competition in Chicago, IL, USA, in 2008. He served as the Chair for the 16th MicroRad 2020 virtual meeting and in the local organizing committee of the 10th Microrad, Florence, in 2008, and the Microwave Signature Symposium of the URSI Commission-F, Florence, in 2010. He participated in the Italian Antarctic Expeditions, carrying out his research at Concordia Station (Dome-C) and Mario Zucchelli Station (Ross Sea) in 2013, 2015, and 2018.

Open Access funding provided by 'Consiglio Nazionale delle Ricerche-CARI-CARE-ITALY'
within the CRUI CARE Agreement